Landslide Risk Assessment along Roads by Using Radar-driven Land Deformation and Rainfall Data

Yoshie Ishii[1], Junichi Susaki[1], Akane Kurihara[1], Tetsuharu Oba[2], Kosei Yamaguchi[3], Yuusuke Miyazaki[4], Kiyoshi Kishida[1]

[1] Department of Civil and Earth Resources Engineering, Graduate School of Engineering, Kyoto University, Kyoto, Japan
{ishii.yoshie.4k; susaki.junichi.3r; kurihara.akane.68j; kishida.kiyoshi.3r}@kyoto-u.ac.jp
[2] Graduate School of Management, Kyoto University, Kyoto, Japan - oba.tetsuharu.5n@kyoto-u.ac.jp
[3] Disaster Prevention Research Institute, Kyoto University, Kyoto, Japan - yamaguchi.kosei.5r@kyoto-u.ac.jp
[4] Faculty of Environmental and Urban Engineering, Kansai University, Osaka, Japan - y.myzk.x@kansai-u.ac.jp

Commission III, WG III/3

Key words: Traffic regulation, land deformation, precipitation**, **spatio-temporal statistical modeling, time-series SAR analysis

Abstract:

To prevent damage from landslide disasters, traffic regulation based on records is implemented before disasters occur in Japan. Logistics and accordingly economic activities are halted once the traffic regulation is implemented. There are problems that the operation of the traffic regulation tends to be redundant in terms of temporal duration and spatial coverage. In this paper, to consider the effect of topography and land deformation and resolve the problems of redundant traffic regulation, we attempted to predict the land deformation using spatio-temporal statistical models whose objective variable was deformation estimated PSInSAR and explanatory variables were accumulated rainfall and maximum gradient angle. Three statistical models: low-rank GP model, separable covariance model, and product-sum covariance model were used. According to the results of experiments, three spatio-temporal models showed similar predictions; relatively small deformations were well fitted while relatively large deformations were poorly fitted. Since land deformation due to landslides is relatively large, it should be considered the measures to improve the prediction of larger deformations.

1. Introduction

In Japan, approximately a thousand landslide disasters occur every year (Ministry of Land, Infrastructure, Transport and Tourism (MLIT), 2024). To prevent damage from landslide disasters, traffic regulation based on records is implemented before the disasters occur. Logistics and accordingly economic activities are halted once the traffic regulation is implemented. There are problems that the operation of the traffic regulation tends to be redundant in terms of temporal duration and spatial coverage. One of the reasons for these problems is considered as the lack of information to predict landslide disasters. i.e. the conventional criterion of traffic regulation is fundamentally based on the accumulated rainfall, and other information such as topography and land deformation are not sufficiently considered. Therefore, if other information that may be related to landslides can be taken into account, it is expected that redundant traffic restrictions in terms of time and space can be reduced.

This research is positioned as an intermediate step toward the goal of reducing redundant traffic regulations and aims to clarify how accurately land deformation can be predicted from rainfall and surface slope.

In this study, we attempt to predict land deformation using models based on spatio-temporal geostatistics. Spatio-temporal geostatistics is a powerful method and its usefulness has been demonstrated in various fields (Idir et al., 2021; Varouchakis et al., 2022; Johnson et al., 2023). There have been some studies using spatio-temporal geostatistics on landslide prediction, but they are still not sufficient. In the previous studies, spatio-temporal variations of landslide susceptibility via space-time binomial Generalized Additive Model (GAM) were estimated (Wang et al., 2024). That research presents a unique example of such a modeling routine and offers a potential standard for

administrations to make informed decisions regarding future urban development (Wang et al., 2024). In another study, three spatio-temporal statistical models: the low-rank Gauss Process (GP), separable covariance model, and product-sum covariance model were used for constructing the land deformation prediction model (Susaki and Kakinami, 2023).

In this research, we apply the above three spatio-temporal models to land deformation prediction following the method mentioned in (Susaki and Kakinami, 2023). However, the explanatory variables differ from the previous research. While, water-related products, precipitation, total soil moisture, and surface runoff selected from Today's Earth Japan which is a land-surface and river-routing model were used as explanatory variables in (Susaki and Kakinami, 2023), we use the eXtended RAdar Information Network (XRAIN), high-frequency observation and high special resolution weather radar as rainfall information and use maximum gradient angle provide by MLIT as topography information. For the objective variable, ground deformation, the Phased Array type L-band Synthetic Aperture Radar-2 (PALSAR-2) onboard the Advanced Land Observing Satellite-2 (ALOS-2) images from which the PSInSAR (Persistent Scatterer Interferometric SAR) analysis was performed are used. The L-band SAR which can permeate leaf and branch is effective in observing the ground surface conditions and therefore land deformation in mountainous regions. There are a lot of studies regarding to monitoring landslide deformations using PALSAR2 images (Sato and Une, 2016; Hao et al., 2019; Liu et al., 2020).

The remainder of this paper is organized as follows. The location and data used for the research are described in Sections 2 and 3, respectively. Section 4 explains the existing spatiotemporal statistical models. Section 5 reports the experimental results including the time-series SAR analysis results and the preprocessing results of water-related products. The implications

of these results are then discussed in Section 6. Finally, Section 7 concludes the paper.

2. Study area

The selected study area was the road section in National Route 9: Kamikizaki-cho, Sonobe-cho, Nantan City - Shinmito, Kyotanba-cho, Funai-gun, and Kyotanba-cho. The red rectangle in Figure 1 shows the study area. It is in mountainous areas and located in Nantan-city, Kyoto Prefecture. In this area, a traffic regulation section is set, which is approximately 4 km long. The section is closed when continuous rainfall is over 230 mm by Kyoto National Highway Office, Kinki Regional Development Bureau, MLIT. MLIT induces a unique accumulation way of rainfall; the hourly rainfall is accumulated until the hourly rainfall of 2 mm/h or less is observed for more than 3 consecutive hours. The consecutive reference values are respectively determined based on the hazard characteristics in the monitored road sections. The geographical age of this traffic regulation section is the Mesozoic era. The area includes geologic faults and is occupied by sandstone and mudstone mainly.

Heavy rainfall occurred in a wide range of Japan centered on West Japan from June 28 to July 8, 2018. This heavy rainfall event was caused by typhoon No.7 (Prapiroon) and an active seasonal rain front. Red point in Figure 1 indicates the location where collapse of geo fiber reinforced soil wall occurred by this heavy rainfall event on July 5, 2018. The geolocation of the point is 35.124469°N, 135.4368°E.
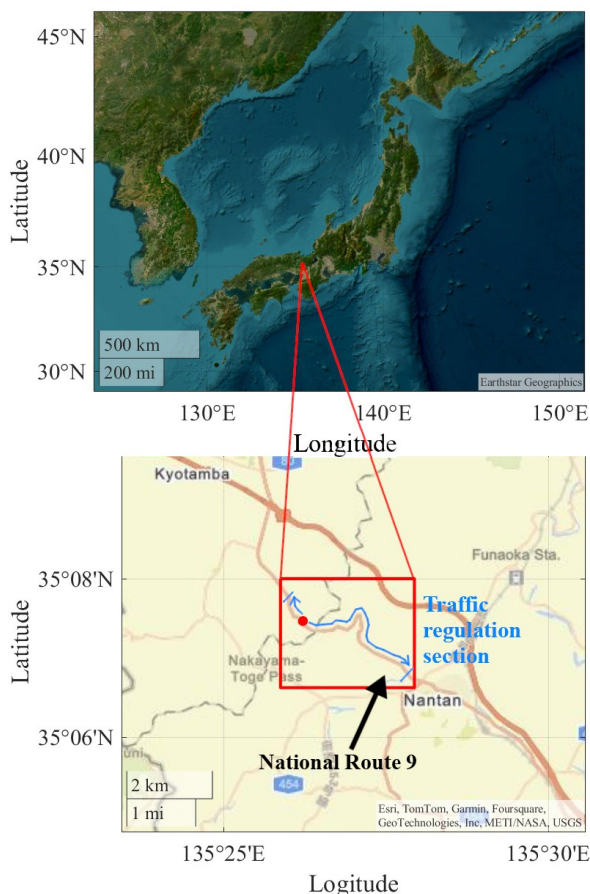

Figure 1. Study area. Red point indicates the location where a collapse of geo fiber reinforced soil wall occurred on July 5, 2018. The background images are from Google Earth (above) and Open Street Map (below).

3. Data Used

3.1 ALOS-2/PALSAR-2

In this research, we used level 1.1 (L1.1) satellite SAR images from the PALSAR-2 instrument onboard the ALOS-2 launched and operated by the Japan Aerospace Exploration Agency (JAXA). Table 1 lists nine PASAR-2 images acquired on the descending orbit and used in this research. The observation mode was UBS, and the observation direction was right.

3.2 GNSS-based control station

Geospatial Information Authority of Japan (GSI) operates approximately 1,300 Global Navigation Satellite System (GNSS)-based Control Stations in Japan. The stations are approximately 10 to 20 km away from each other. GSI publishes daily F5 fix data for free (GSI, n.d.), and we downloaded the data of the Mizuho GNSS-based control station near the study area as shown in Figure 2.

3.3 XRAIN

In Japan, MLIT is operating eXtended RAdar Information Network (XRAIN) system to measure rainfall and utilize the data for weather forecast and disaster prevention. XRAIN uses X-band multi-parameter (MP) radar. Spatial resolution is 250 m and temporal resolution is 1 minute. MP radar is used to determine the shape of raindrops and estimate rainfall based on the flatness of raindrops. As a result, observation data and highly accurate data to be transmitted in real time. Observations began in 2010, and the data have been available since 2018.

3.4 Maximum gradient angle

Topography is considered to affect the land deformation. We used maximum gradient angle information provided by MLIT. The fifth mesh maximum gradient angle created in 2009 was downloaded from the digital national land information download site (https://nlftp.mlit.go.jp/ksj/). According to MLIT the gradient angle was calculated using 50 m mesh elevation which was resampled by 10 m mesh Digital Elevation Model (DEM) provided by GSI.

No.	Observation (yyyy/mm/dd)
1	2017/04/02
2	2017/07/23
3	2017/12/10
4	2018/04/01
5	2018/05/13
6	2018/09/16
7	2018/10/14
8	2018/12/09
9	2019/03/31
10	2019/05/12
11	2019/07/21
12	2019/09/15
13	2019/12/08

Table 1. ALOS-2/PALSAR-2 descending images used for experiments.

4. Method

In this study, we attempt to predict land deformation from rainfall and terrain information based on spatio-temporal geostatistics. In this chapter, we describe the spatio-temporal analyses used for experiments.

Let $y_i(\boldsymbol{s},t)$ $(i = 1,2,\cdots,N)$ denote the land deformation at geolocation $\boldsymbol{s}$ $(\boldsymbol{s} \in D, D \subset R^2)$ and time t $(t \in T, T \subset R)$. Here, $N = mn$, and m is the number of location and n is the number of time. R is the set of real numbers. $\boldsymbol{x}_i = \left(1, x_{i1}(\boldsymbol{s},t), \cdots, x_{ip}(\boldsymbol{s},t)\right)$, $\boldsymbol{\beta} = \left(\beta_0, \beta_1, \cdots, \beta_p\right)^T$, and ε_i $(i = 1,2,\cdots,N)$ are the explanatory variables, the regression coefficients, and the error, respectively. The spatio-temporal kriging model with covariance $c(d_{i,j}, t_{i,j})$ is expressed as

$$
\begin{aligned}
y_i(\boldsymbol{s},t) &= \boldsymbol{x}_i \boldsymbol{\beta} + \varepsilon_i, \\
\varepsilon_i &\sim N\left(0, c(d_{i,j}, t_{i,j})\right), \\
i,j &= 1,2,\cdots,N.
\end{aligned} \tag{1}
$$

Here, $d_{i,j} = \|\boldsymbol{s}_i - \boldsymbol{s}_j\|$, $t_{i,j} = |t_i - t_j|$. In this research, below two patterns of covariance models are considered

$$
\begin{aligned}
c(d_{i,j}, t_{i,j}) &= c(d_{i,j})c(t_{i,j}), \\
c(d_{i,j}, t_{i,j}) &= c(d_{i,j}) + c(t_{i,j}) + kc(d_{i,j})c(t_{i,j}), \\
\text{s.t. } &\textstyle\sum_{i=1}^N \sum_{j=1}^N a_i, a_j c(d_{i,j}, t_{i,j}) > 0, \forall a_i, a_j \in R.
\end{aligned} \tag{2}
$$

The prior is called the separable covariance model with product of $c(d_{i,j})$ and $c(t_{i,j})$, and the latter is called the product-sum covariance model, where k is a coefficient representing the cross-correlation between $c(d_{i,j})$ and $c(t_{i,j})$. The constraint means both $c(d_{i,j})$ and $c(t_{i,j})$ must be positive-definite for any $a_i, a_j \in R$.

The low-rank Gaussian process (GP) model is expressed as

$$
\begin{aligned}
y_i(\boldsymbol{s},t) &= \boldsymbol{x}_i \boldsymbol{\beta} + \eta_i^{(s)} + \eta_i^{(t)} + \eta_i^{(st)} + e_i, \\
e_i &\sim N(0, \sigma^2), \qquad i = 1,2,\cdots,N.
\end{aligned} \tag{3}
$$

Here, e_i is the error. $\eta_i^{(s)}$, $\eta_i^{(t)}$, $\eta_i^{(st)}$ are spatial correlation, temporal correlation, and spatio-temporal cross correlation, respectively. They are expressed as

$$
\eta_i^{(s)} = \textstyle\sum_{j=1}^m \varphi_{j,i}^{(s)} \alpha_j^{(s)}, \quad \alpha_j^{(s)} \sim N(0, \tau_{(s)}^2), \tag{4}
$$

$$
\eta_i^{(t)} = \textstyle\sum_{k=1}^n \varphi_{k,i}^{(t)} \alpha_k^{(t)}, \quad \alpha_k^{(t)} \sim N(0, \tau_{(t)}^2), \tag{5}
$$

$$
\eta_i^{(st)} = \textstyle\sum_{j=1}^m \sum_{k=1}^n \varphi_{j,i}^{(s)} \varphi_{k,i}^{(t)} \alpha_{j,k}^{(st)}, \quad \alpha_{j,k}^{(st)} \sim N(0, \tau_{(st)}^2). \tag{6}
$$

5. Experiments

5.1 Time-series SAR analysis

We implemented PSInSAR analysis (Ferretti et al., 2001) to multi-temporal PALSAR-2 images described in Table 1. We estimated land deformation velocities from descending-orbit images. We used the AW3D (EORC JAXA, n.d.) whose resolution is 30 m as the DEM to calculate the land deformation velocities. We referred to GNSS data obtained at the Mizuho GNSS-based control station of GSI near the study area, as shown in Figure 2.
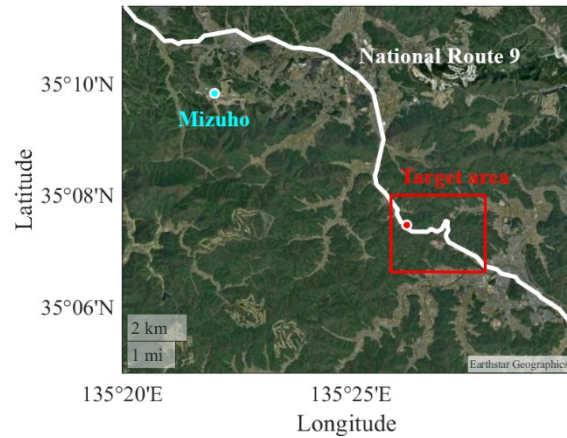

Figure 2. GNSS-based control station near the study area. "Mizuho" is a GNSS-based control station of GSI near the study area. The red point is the location where a collapse of geo fiber reinforced soil wall occurred. The background image is from Google Earth.

In PSInSAR analysis, we set the threshold for F-value in Eq. (7) (Anahara and Shimada, 2017) as -0.95 in order to select stable permanent scatterer (PS),

$$
F = -\left|\textstyle\sum_{m,n} \exp\left(i\left(\phi(t_{mn}) - \hat{\phi}(t_{mn})\right)\right)\right|, \tag{7}
$$

$$
\phi(t_{mn}) = \frac{4\pi}{\lambda} v(t_n - t_m)\cos\theta + \frac{4\pi}{\lambda r \sin\theta} \Delta Z B_\perp, \tag{8}
$$

where m and n are scene number, t is acquisition time, ϕ is observed interferometric phase, λ is wavelength, v is deformation rate, θ is incidence angle, r is slant range, ΔZ is DEM error height, $B_\perp$ is perpendicular baseline.

We extracted the PSs available during all the periods. Multiplying the deformation rate by time between two SAR observations, we generated the relative land deformation map. The land deformation obtained was along the line of sight and then was converted into the vertical deformation by dividing by the cosine of the radar incident angle. For each 250 m grid, the average of the deformation of the PS points in it was taken. An example of the relative land deformation map at the 250 m grid is shown in Figure 3(a). The period is from May 13 to September 16, 2018.

In order to match the period to XRAIN X-band data, only 9 periods of deformation data from April 1, 2018, to December 8, 2019, were used for spatio-temporal analysis. On the other hand, at least 10 periods of data are required to conduct spatio-temporal analysis using the R library. To treat this issue, the linear interpolation for each of the two periods was calculated. Consequently, 17 periods of deformation images were used for spatio-temporal analysis as shown in Table 2.
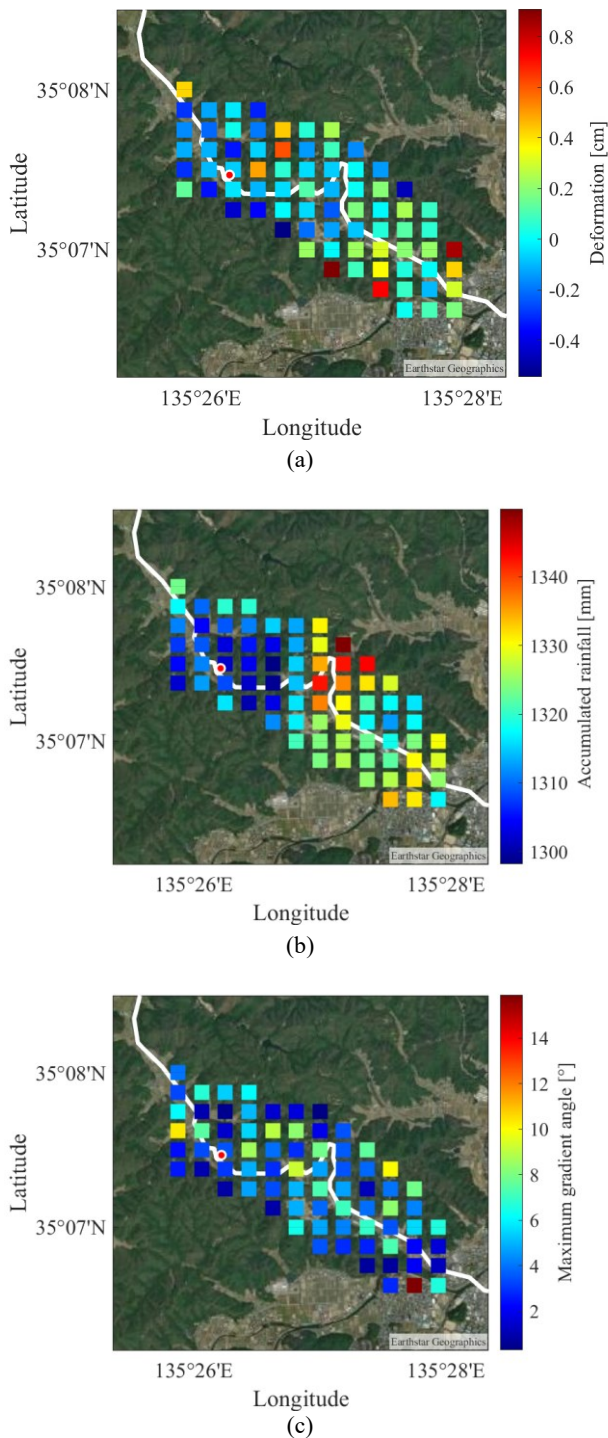
(a)

(b)

(c)

Figure 3. (a) Example of the relative deformation map from May 13 to September 16, 2018. While positive values indicate the amount of uplift, negative values indicate the amount of subsidence. (b) Example of the accumulated rainfall map from May 13 to September 16, 2018. (c) Maximum gradient angle map. The red point is the location where a collapse of geo fiber reinforced soil wall occurred. The background image is from Google Earth.

5.2 XRAIN

We calculated the accumulated rainfall using XRAIN within a period of two satellite image observations. An example of the accumulated rainfall map at the 250 m grid is shown in Figure

3(b). The period is from May 13 to September 16, 2018. After that, the linear interpolation of the accumulated rainfall data was conducted in the same way as the SAR images.

5.3 Maximum gradient angle

The maximum gradient angle was used as a consistency value throughout the period from April 1, 2018, to October 27, 2019. Figure 3(c) indicates the maximum gradient angle map in the target area.

5.4 Descriptive modeling

The accumulated rainfall and maximum gradient angle were normalized by subtracting the mean and dividing by the standard deviation before entering the descriptive models.

We used **vgmST** in R to construct a spatio-temporal variogram. Parameters for product-sum model were set to $\tau^2 = 0.06, \sigma^2 = 0.012, r = 0.004$ for space and $\tau^2 = 0.06, \sigma^2 = 0.012, r = 500$ for time, and k=0.5. Parameters for separable model were set to $\tau^2 = 0.06, \sigma^2 = 0.012, r = 0.004$ for space and $\tau^2 = 0.06, \sigma^2 = 0.012, r = 500$ for time, and $sill$=0.07.

We used **mgcv** in R for the low-rank GP model. We set the function as

$$Defo \sim te\big(X, Y, Time, k = c(7,15), d = c(2,1)\big) + s(Time) + s(XRAIN) + s(Slope), \quad (9)$$

where the function te forms the product of X, Y, and $Time$, the "7" and "15" in $c(7,15)$ are the numbers of basis functions in space and time, respectively. To decide the optimal parameter, we conducted grid search for $c(7,15)$ in the range of [5, 50] for space and in the range of [3, 20] for time. The "2" and "1" in $c(2,1)$ are the dimensions in space and time, respectively, and the function s represents the spline smoothing function.

No.	Period (yyyy/mm/dd - yyyy/mm/dd)
1	2018/04/01 - 2018/04/22
2	2018/04/22 - 2018/05/13
3	2018/05/13 - 2018/07/15
4	2018/07/15 - 2018/09/16
5	2018/09/16 - 2018/09/30
6	2018/9/30 - 2018/10/14
7	2018/10/14 - 2018/11/11
8	2018/11/11 - 2018/12/09
9	2018/12/09 - 2019/02/03
10	2019/02/03 - 2019/03/30
11	2019/03/30 - 2019/04/21
12	2019/04/21 - 2019/05/12
13	2019/05/12 - 2019/06/16
14	2019/06/16 - 2019/07/21
15	2019/07/21 - 2019/08/18
16	2019/08/18 - 2019/09/15
17	2019/09/15 - 2019/10/27

Table 2. Periods used for spatio-temporal analysis

	Low-rank gauss	Product–sum	Separable
RMSE [cm]	0.218	0.235	0.221

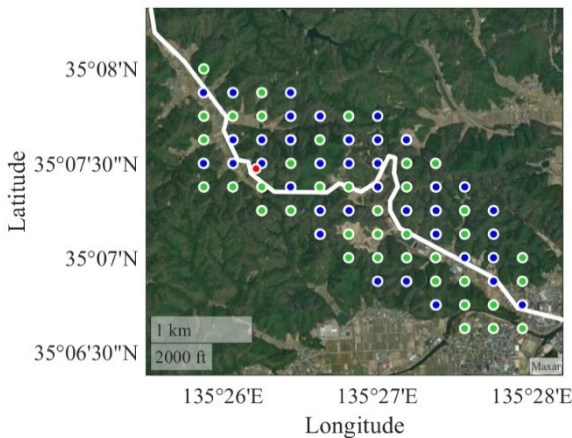Table 3. Results of applying spatio-temporal models to validation.

Figure 4. Green points were used for modeling. Blue points were used for validation. The red point is the location where a collapse of geo fiber reinforced soil wall occurred. The background image is from Google Earth.

The 250 m grids are separated into one class for modeling and another for validation as shown in Figure 4.

Table 3 gives the statistics of the validation results, orange points in Figure 5 show the geolocations of characteristic points, and Figure 6 shows the temporal deformations measured and predicted by three descriptive models, i.e., a low-rank GP model, a product–sum covariance model, and a separable variance model.
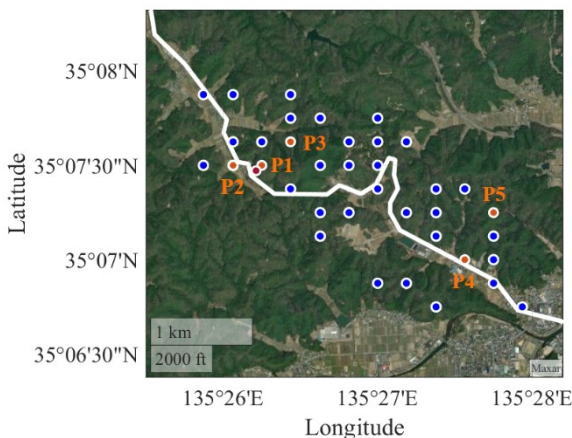

Figure 5. Geolocations of regions of interest (ROIs). The red point indicates the geolocation where a collapse of geo fiber reinforced soil wall occurred. Blue and orange points were used for validation. In particular, orange points indicate the geolocation of the examples shown in Figure 6. The background image is from Google Earth.

6. Discussion

The period of Figure 3(a), from May 13 to September 16, 2018, includes the date, July 5, 2018, when the collapse of geo fiber reinforced soil wall occurred. However, the locations near where the disasters occurred do not show particularly large deformation compared to other locations. It is difficult to identify the reason from only this result, but we can consider that the land deformation can't be captured because of occurring the deformation at the nonsensitive direction for SAR, the deformation may have been captured at the PSInSAR process but cancelled out by spatial smoothing, and so on.

Figure 6 shows the characteristic results and the geolocation of each graph corresponding to Figure 5. Figure 6(a) is the nearest point to the location where a collapse of geo fiber reinforced soil wall occurred. Figure 6 (b)(c)(d)(e) show the examples of better fitting and worse fitting near and far from the location where a collapse of geo fiber reinforced soil wall occurred to data measured. From these results, we can confirm that the similar results were obtained from three descriptive spatio-temporal models. This trend is also shown as similar RMSE values in Table 3. There is no difference whether near or far from the location where a collapse of geo fiber reinforced soil wall occurred. We can consider that the difference between better fitting and worse fitting is whether the measured deformation is relatively smaller or larger. That is, relatively small deformations are well fitted while relatively large deformations are poorly fitted. Since land deformation due to landslides is considered to be relatively large, it should be considered the measures to improve the prediction of larger deformations.

In order to improve prediction accuracy, the following issues need to be considered in future works. First, we need to search for the optimal explanatory and objective variables. In this study, we only consider the accumulated rainfall for two SAR images period. It means we considered the factor of long period accumulated rainfall. However, short time period of accumulated rainfall such as 60 minutes accumulated rainfall and 72 hours of accumulated rainfall are considered important factors (Yamamoto, 2019). Therefore, it may be valuable to consider the short time period of rainfall.

In addition, it is said that landslides are related to various factors such as geological features, vegetation, underground water, diastrophism, and earthquakes, even apart from rainfall and slope. There are some factors that are not easy to consider because of the difficulty of the observation. Therefore, we should try to consider how to take in these factors as explanatory variables directly and indirectly. For land deformation information using SAR images, only vertical deformation was considered in this experiment. However, land deformation is not always vertical direction. Thus, we need to calculate 3-dimensional deformation to analyze the land deformation close to reality.

Second, the number of data, especially, the spatial spread should be increased. In this experiment, only 39 locations were used for constructing of spatio-temporal models. Therefore, it may be insufficient to grasp the spatial trend accurately.

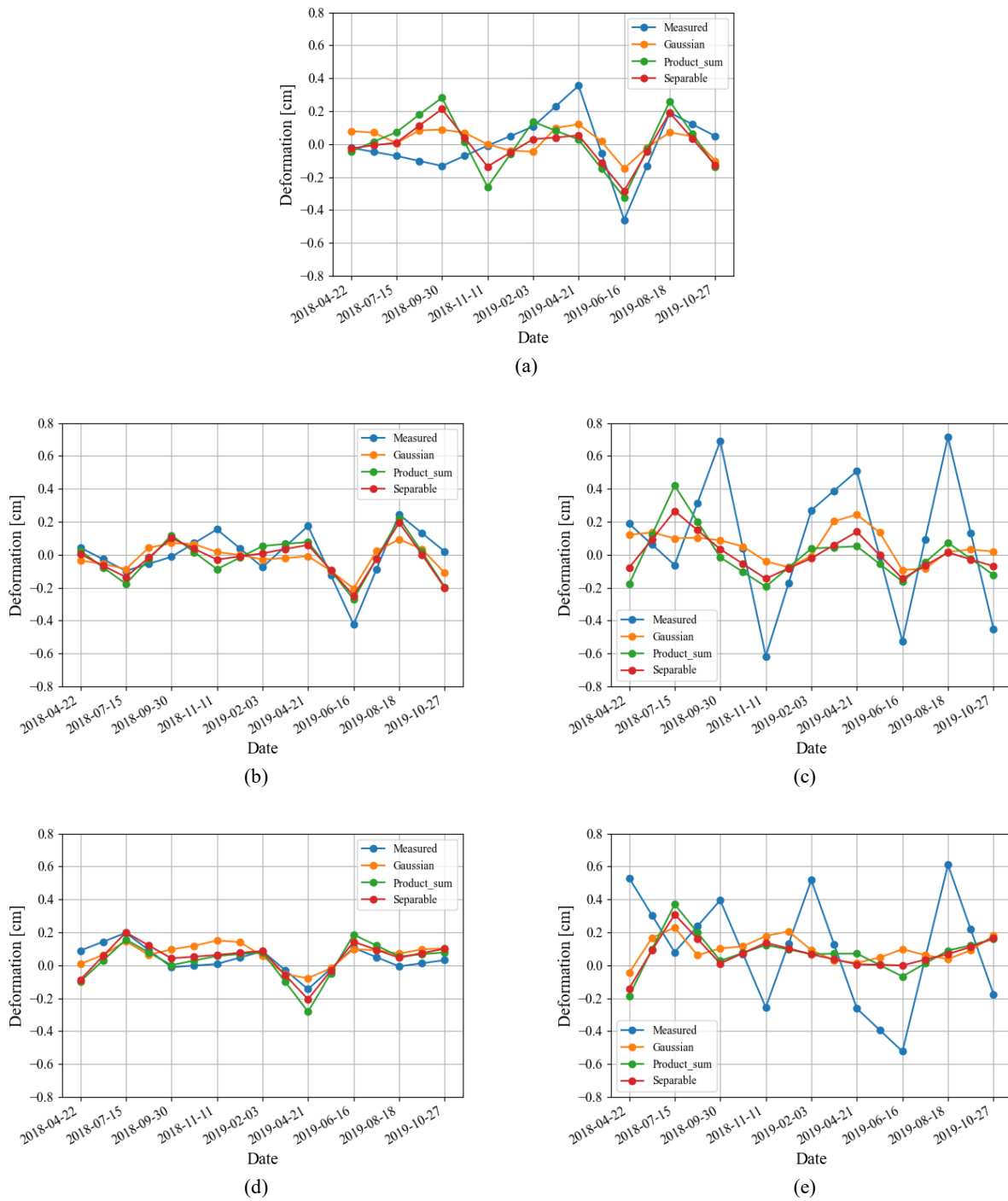(a)

(b)

(c)

(d)

(e)

Figure 6. Temporal deformations estimated by spatio-temporal models: (a) corresponds to P1 in Figure 5. This is the nearest location where a collapse of geo fiber reinforced soil wall occurred.; (b) corresponds to P2 in Figure 5. This is an example that is near P1 and better model fitting; (c) corresponds to P3 in Figure 5. This is an example that is near P1 and worse model fitting; (d) corresponds to P4 in Figure 5. This is an example that is far from P1 and better model fitting, and (e) corresponds to P5 in Figure 5. This is an example that is far from P1 and worse model fitting.

The objective of this study was to clarify how accurately land deformation can be predicted from rainfall and surface slop using a spatio-temporal model to achieve spatial and temporal optimization of road traffic restrictions. Although it would be challenging to optimize road traffic control based on the results obtained in this study only, investigating more detailed conditions such as 3-dimensional deformation analysis of SAR and analysis of XRAIN with various time resolutions could possibly contribute to that goal.

7. Conclusions

In this paper, we attempted to predict the land deformation using spatio-temporal statistical models whose objective variable was deformation estimated by PSInSAR and explanatory variables were accumulated rainfall and maximum gradient angle. Three statistical models: low-rank GP model, separable covariance model, and product-sum covariance model were used. The target area was set to the road section in National Route 9 in Japan. The area caused a collapse of geo fiber reinforced soil wall on July 5, 2018. According to the results of experiments, three spatio-temporal models showed similar predictions; relatively small deformations were well fitted while relatively large deformations were poorly fitted. Since land deformation due to landslides is considered to be relatively large, it should be considered the measures to improve the prediction of larger deformations.

Acknowledgements

References

Anahara, T., Shimada, M., 2017. Inter-sensor analysis of persistent scatterer L-band SAR interferometry. *2017 IEEE International Geoscience and Remote Sensing Symposium (IGARSS)*, 2438-2441. doi: 10.1109/IGARSS.2017.8127485.

EORC, JAXA, n.d.: ALOS World 3D - 30m (AW3D30) data set, https://www.eorc.jaxa.jp/ALOS/en/dataset/aw3d30/aw3d30_e.htm (18 April 2024).

Ferretti, A., Prati, C., Rocca, F., 2000. Nonlinear subsidence rate estimation using permanent scatterers in differential SAR interferometry. *IEEE Trans. Geosci. Remote Sen.,* 38(5), 2202–2212. doi: 10.1109/36.868878.

Takamatsu, N., Muramatsu, H., Abe, S., Hatanaka, Y., Furuya, T., Kakiage, Y., Ohashi, K., Kato, C., Ohno, K., Kawamoto, S., 2023. New GEONET analysis strategy at GSI: daily coordinates of over 1300 GNSS CORS in Japan throughout the last quarter century. *Earth Planets Space*, 75(1):49. doi.org/10.1186/s40623-023-01787-7.

Hao, J., Wu, T., Wu, X., Hu, G., Zou, D., Zhu, X., Zhao, L., Li, R., Xie, C., Ni, J., Yang., C., Li, X., Ma, W., 2019. Investigation of a small landslide in the Qinghai-Tibet Plateau by InSAR and absolute deformation model. *Remote Sensing*, 11(18), 2126. https://doi.org/10.3390/rs11182126.

Idir, Y. M., Orfila, O., Judalet, V., Sagot, B., Chatellier, P., 2021. Mapping urban air quality from mobile sensors using spatio-temporal geostatistics, *Sensors*, 21(14), 4717. https://doi.org/10.3390/s21144717.

Johnson, O., Giorgi, E., & Asfaw, Z. G., 2023. Understanding the importance of spatial correlation in identifying spatio-temporal variation of disease risk, in the case of malaria risk mapping in southern Ethiopia. *Scientific African*, 22. https://doi.org/10.1016/j.sciaf.2023.e01926.

Liu, X., Zhao, C., Zhang, Q., Lu, Z., Li, Z., 2020. Deformation of the Baige landslide, Tibet, China, revealed through the integration of cross-platform ALOS/PALSAR-1 and ALOS/PALSAR-2 SAR observations, *Geophysical Research Letters*, 47(3). https://doi.org/10.1029/2019GL086142.

Ministry of Land, Infrastructure, Transport and Tourism (MLIT), Sediment-related disasters in 2023, https://www.mlit.go.jp/river/sabo/jirei/r5dosha/r5dosyasaigai.pdf (16 July 2024, in Japanese).

Sato, H. P., Une, H., 2016. Detection of the 2015 Gorkha earthquake-induced landslide surface deformation in Kathmandu using InSAR images from PALSAR-2 data. *Earth, Planets and Space,* 68(47), 1-13. https://doi.org/10.1186/s40623-016-0425-1.

Susaki, J and Kakinami, R. 2023. Modeling land deformations in mountains by combining time-series L-band SAR images and spatiotemporal statistical models. *ISPRS Annals of the Photogrammetry, Remote Sens. Spatial Inf. Sci.*, X-1/W1-2023, 731-738. https://doi.org/10.5194/isprs-annals-X-1-W1-2023-731-2023.

Wang, T., Dahal, A., Fang, Z., van Westen, C., Yin, K., Lombardo, L., 2024. From spatio-temporal landslide susceptibility to landslide risk forecast. *Geoscience Frontiers,* 15(2). https://doi.org/10.1016/j.gsf.2023.101765.

Varouchakis, E. A., Guardiola-Albert, C., & Karatzas, G. P., 2022. Spatiotemporal geostatistical analysis of groundwater level in aquifer systems of complex hydrogeology. *Water Resources Research*, 58(3). https://doi.org/10.1029/2021WR029988.

Yamamoto, H., Kawamoto, E., Watanabe, Y., Nasu, M., Sakamoto, K. and Iwaya, K., 2019. Change of the land use and characteristics of landslide disaster by heavy rainfall in July 2018, *J. Japan Soc. Natural Disaster Sci.*, 38(2), 185-205. https://doi.org/10.24762/jndsj.38.2_147 (in Japanese).